Crack imaging by scanning pulsed laser spot thermography

Teng Li, Darryl P. Almond *, D.Andrew S. Rees

UK Research Centre in NDE (RCNDE), Department of Mechanical Engineering, University of Bath, Claverton Down, Bath BA2 7AY, UK

ABSTRACT

A new crack imaging technique is presented that is based on second derivative image processing of thermal images of laser heated spots. Experimental results are shown that compare well with those obtained by the dye penetrant inspection method. A 3D simulation has been developed to simulate heat flow from a laser heated spot in the proximity of a crack. A 'ghost point' method has been used to deal efficiently with cracks having openings in the micometre range. Results are presented showing the effects of crack geometry and system parameters on thermal images of laser heated spots.

© 2010 Elsevier Ltd. All rights reserved.

1. Introduction

Pulsed thermography (PT) is a non-contact, quick inspection method that detects in-plane defects such as delaminations and impact damage [1–4]. It is a technique that is not suitable for the detection of important surface breaking cracks in metals caused by fatigue or creep. These cracks, which grow predominantly perpendicular to the material surface, typically have openings of a few microns. It has been reported that surface cracks with openings (widths) of below 0.5 mm on a concrete surface could not be detected by PT [5]. In the laser spot thermography (LST) technique, a laser provides a highly localized heating spot. Heat flow in the volume of the material from such a spot presents a relatively symmetrical half-spherical shape in the radial directions if the material is thermally isotropic. Perpendicular cracks, close to the heated spot, will perturb the round lateral heat flow and the perturbation may be detected by a thermal camera to reveal the cracks. Preliminary studies [6–14] showed that the shape of the heat flow at certain times was deformed clearly by perpendicular cracks. Based on the previous studies, a full 3D 'ghost point' heat transfer finite difference model has been developed to predict the thermal behaviour of laser spot heated material in the proximity of a crack. Furthermore, a new image processing technique has been developed to form a direct image of a crack.

2. 'Ghost point' heat diffusion model

Modelling has been used to gain an understanding of the optimum operating parameters for the laser spot thermography technique and to assess the theoretical limits of its sensitivity for the detection of cracks. The effects of cracks may be simulated by 'ghost points' in a numerical modelling grid that are generated by balancing thermal fluxes flowing into a crack and through a crack, with those flowing out of the crack according to Fourier's law. They guarantee correct thermal gradients in the bulk material on either side of the crack.

The concept of the 'ghost point' in a 1D finite difference heat transfer model is shown in Fig. 1. In this case, the crack is embedded between the current grid point 'i' and its left grid point '$i-1$'. The width of the crack 'δ' may be far smaller than the grid spacing 'd'. The distance of the crack to the left grid point is 'σ'. Usually, the crack is full of air and its conductivity 'K_a' is much lower than the conductivity of the metal block 'K_s'. Thus thermal gradient across the crack will be larger than in other parts of the metal block.

Heat flux balance in the x direction when it flows from the grid point '$i-1$' into the crack, through the crack, and then flows out of the crack to the grid point 'i' gives

$$K_s \frac{T_L - T_{i-1}}{\sigma} = K_a \frac{T_R - T_L}{\delta} = K_s \frac{T_i - T_R}{d - \sigma - \delta} = g \qquad (1)$$

where T_{i-1}, T_L, T_R, T_i and T_{i+1} are, respectively, the temperature rise at the grid point '$i-1$', the left boundary of the crack, the right boundary of the crack and the grid points of 'i' and '$i+1$'; g is the heat flux.

Eq. (2) shows the calculation of temperature rise at the 'ghost point'. By defining a 'ghost point' to equal the temperature

* Corresponding author.
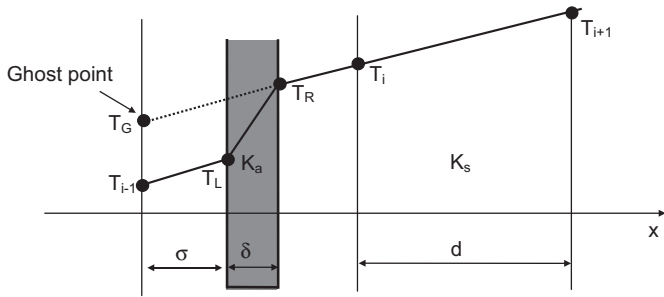E-mail address: D.P.Almond@bath.ac.uk (D.P. Almond).

Fig. 1. 1D 'ghost point' finite difference heat diffusion model. Heat flux is balanced when it flows into, through and out of the crack.

increase effect because of the crack, the 'isotropic' heat transfer model can still be applied; however, temperature rise at the grid point '$i-1$' should be replaced by the value of the 'ghost point' T_G:

$$K_s \frac{T_i - T_G}{d} = g \qquad (2)$$

After substituting Eq. (1) in Eq. (2), we can represent T_G by T_i and T_{i-1}:

$$T_G = \frac{\xi}{\xi + d} T_i + \frac{d}{\xi + d} T_{i-1} \qquad (3)$$

where ξ is related with K_s, K_a and δ:

$$\xi = \left(\frac{K_s}{K_a} - 1 \right) \delta \qquad (4)$$

The 1D heat diffusion equation with no internal heat generation is

$$k \frac{\partial^2 T}{\partial x^2} = \frac{\partial T}{\partial t} \qquad (5)$$

where k is the thermal diffusivity. Substituting Eq. (3) in Eq. (5), and representing Eq. (5) using finite difference elements, we can have

$$T_i^{m+1} = \frac{k \Delta t}{2d} (T_{i+1}^m - a T_i^m + b T_{i-1}^m) + T_i^m \qquad (6)$$

where Δt is the time step, T_i^m the temperature rise of the grid point 'i' at time m and T_i^{m+1} the temperature rise at the next time step. The values of a and b are

$$a = \frac{\xi + 2d}{\xi + d} \qquad (7)$$

$$b = \frac{d}{\xi + d} \qquad (8)$$

If the heat diffusion model is 2D, then the value of a becomes

$$a = \frac{3\xi + 4d}{\xi + d} \qquad (9)$$

Similarly, in the 3D heat diffusion model, a has the value

$$a = \frac{5\xi + 6d}{\xi + d} \qquad (10)$$

If the crack is embedded between current grid point i' and point '$i+1$', then grid point '$i+1$' becomes the 'ghost point' and temperature rise at this point should multiply the coefficient b like the ghost point '$i-1$' in Eq. (6).

Furthermore, the temperature gradient across the crack can also be derived from Eq. (1) as follows:

$$\frac{T_R - T_L}{\delta} = \frac{T_i - T_{i-1}}{K_a / K_s (d - \delta) + \delta} \qquad (11)$$

By using the 'ghost points' to balance the heat flux, the heat transfer model avoids the need of very fine mesh spacing that is necessary to deal with real cracks that often have openings of only a few micrometres [6,7]. In the following simulations, the boundary conditions for all metal samples are assumed to be insulated. Table 1 shows the property parameters used in the simulations for the air gap and two types of steel.

3. Experimental and modelling results

3.1. Modelling validation

Previous publications using the 2D ghost point method [6,7] gave an indication of the way in which defect opening and host material affect LST response. In this research, a full 3D ghost point model was developed to enable a comprehensive investigation of all factors that affect the response of the technique. A further difference is that a much higher power laser was used in the current work. The previous work [6,7] was completed using laser powers of < 1 W, whilst in the current work a 21 W Laservall industrial fibred diode welding/brazing laser has been used. The laser beam wavelength is 808 nm and its focal spot diameter is about 1.8 mm. The laser is operated in a pulse mode. The pulse width can be set from 1 ms to 10 s.

Fig. 2 shows the experimental setup. A computer is used to control the translation stage to move either the test-piece or the laser head (Fig. 2 shows only one arrangement). The computer also controls the laser output power and pulse duration. The infrared camera used to record the thermal images was a Merlin MID (Indigo Systems Cooperation) with a frame rate of 60 Hz. Thermal images are stored into a second computer for post-processing.

Fig. 3a shows a mild steel test-piece (painted with black paint on the surface) with a fatigue crack developed vertically at the tip of a T-notch. The crack opening (width) is about 50 µm, length is about 5 mm and depth is about 4 mm. Fig. 3b shows the resulting thermal contour images obtained after subtracting the background thermal image. The first 9 frames are shown after a 13 W laser spot heating

Table 1
Parameters used in the simulations.

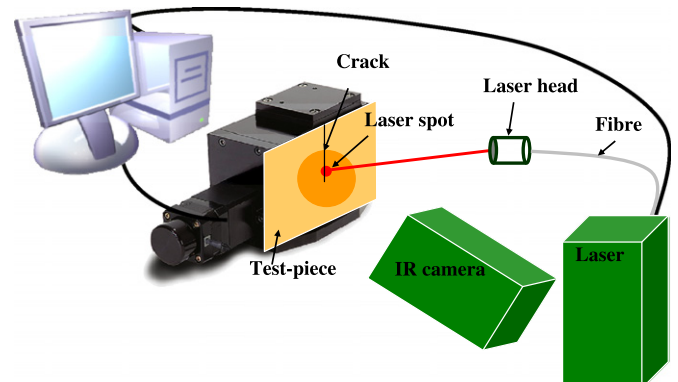| Material	Thermal conductivity K (W/m K)	Specific heat C (J/kg K)	Mass density ρ (kg/m³)	Thermal diffusivity $k = K/\rho C$ (m/s²)
Air	0.025	1000	1.205	2.0747×10^{-5}
Mild steel	40	500	7850	1.0191×10^{-5}
Stainless steel	13.5	485	7900	3.5234×10^{-6}

Fig. 2. Experimental setup.

with a duration of 50 ms irradiated at the right hand side of the crack (about 1 mm from the laser spot centre to the crack). The first 3 frames show the time when the laser was still on. From the 4th frame, the laser spot was switched off and the heat started to dissipate across the test-piece. The effect of thermal resistance of the air-filled crack is to cause thermal flows, evident in the images, to form a 'D' shape rather than a round shape. It can also be seen that the full extent of the crack becomes clearer with elapsed time. Fig. 3c shows corresponding simulated thermal contour images using a Gaussian shape pulse. Note here, temperature rise scales in Fig. 3b are in IR camera 'digital level' units and in Fig. 3c are in units of degrees Celsius. The conversion factor is around 300. There is a very good agreement between the sets of experimental and simulated thermal images.
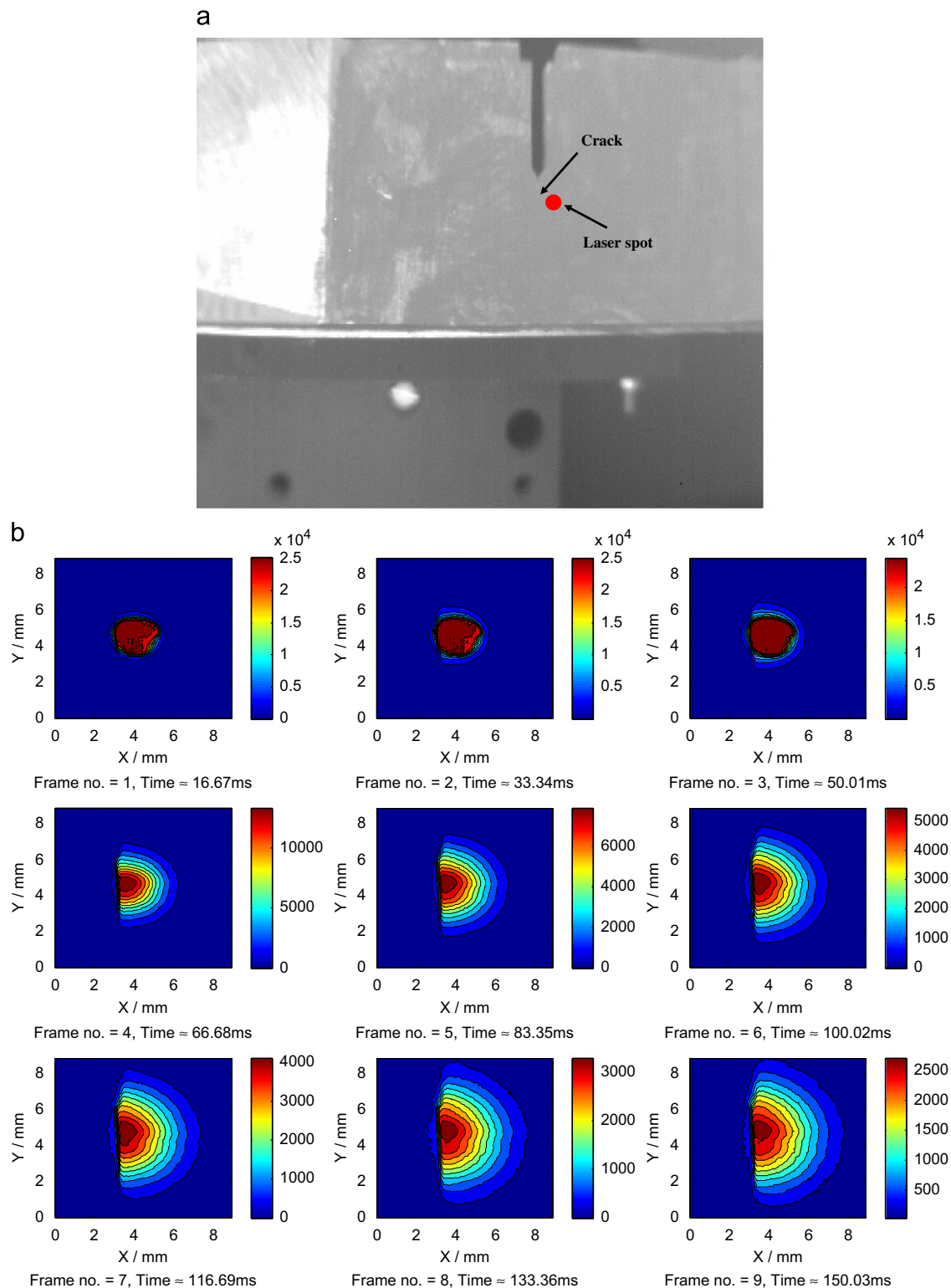

Fig. 3. (a) Mild steel test-piece with a crack at the tip of a T-notch. (b) Resulting experimental thermal contour images. Temperature rise scales are in 'digital level' units. (c) Corresponding simulated thermal contour images. Temperature rise scales are in degrees Celsius.
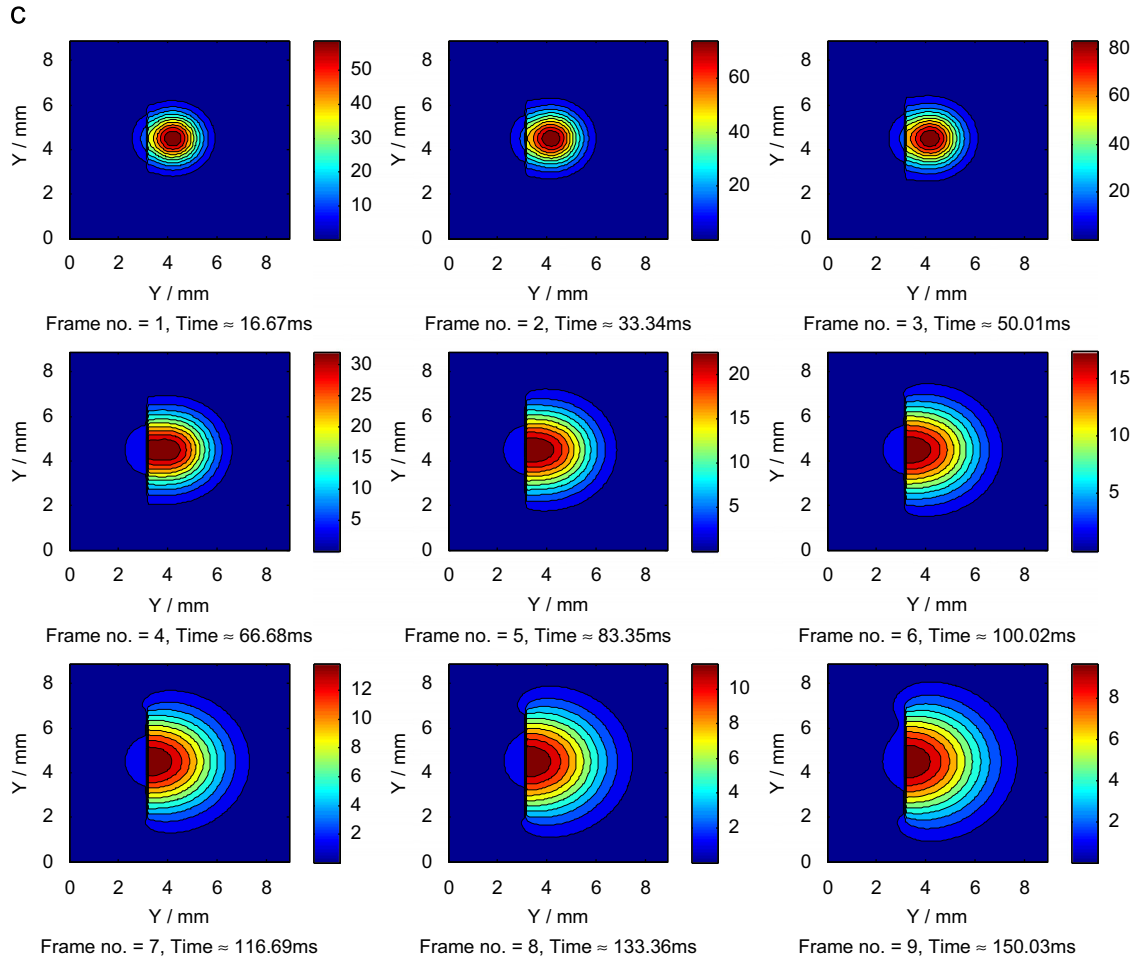
C

Frame no. = 1, Time ≈ 16.67ms   Frame no. = 2, Time ≈ 33.34ms   Frame no. = 3, Time ≈ 50.01ms

Frame no. = 4, Time ≈ 66.68ms   Frame no. = 5, Time ≈ 83.35ms   Frame no. = 6, Time ≈ 100.02ms

Frame no. = 7, Time ≈ 116.69ms   Frame no. = 8, Time ≈ 133.36ms   Frame no. = 9, Time ≈ 150.03ms

Fig. 3. (Continued)

Eq. (12) shows the 3D analytical solution of temperature distribution using Duhamel's theorem in a semi-infinite metal block after the irradiation of a laser spot [15]:

$$T(r,z,t) = \frac{I_{max} r_a^2 k^{1/2}}{K \pi^{1/2}} \int_0^t \frac{p(t-t') \exp(-z^2/4kt' - r^2/(4kt' + r_a^2))}{t'^{1/2}(4kt' + r_a^2)} dt' \tag{12}$$

where, (r,z) are cylindrical coordinates with the origin on the surface at the centre of the irradiated spot. I_{max} is the maximum power density of the laser pulse, $p(t)$ the normalized temporal profile of the laser pulse at time t, k the diffusivity, K the conductivity and r_a the laser beam radius.

Fig. 4 shows a comparison of the 3D analytical modelling results and the 3D ghost point modelling results. The laser pulse was of square shape (50 ms) in the time domain and Gaussian shape in the spatial domain. The radius of the spot was taken to be 1 mm ($1/e$ fall and $r_a = 1$ mm). Laser output power was 20 W; thus, $I_{max} \approx 20/(\pi r_a^2) \approx 6.37 \times 10^6$ W/m². The width of the crack 'δ' in the ghost point model was set to 0 since Eq. (12) is for an isotropic metal block. Note here that reflectivity of the sample surface was not considered in both models, that is, all 20 W energy was assumed to be absorbed by metal samples. Lines with different colors in the figures correspond to temperature rises of the laser spot centre at different depths in the metal block. Differences between the two curves are very small, caused by several factors: boundary conditions of the 3D numerical model and 'accuracy' of the 3D numerical model, such as time step, space step and different numerical methods. The numerical model

here produces a good approximation to the analytical model, which validates the model.

Fig. 5a shows the experimental results obtained using a laser spot, with radius of about 1 mm, irradiated on a mild steel surface for 50 ms with powers between 12 and 20 W, indicated in the figure. The reflectivity of the sample surface was about 60%. The graph shows measurements obtained at 1/60 s time intervals, corresponding to the 60 Hz frame rate of the IR camera. Maximum temperature rises (corresponding to temperature rises at the laser spot centre) are shown. Fig. 5b shows the 3D ghost point finite difference modelling results. Temperature rises after cooling time 50 ms under different laser power irradiations in experiments (Fig. 5a) are less distinguishable than theoretical curves (Fig. 5b) because of the sensitivity of the IR camera and thermal noise at room temperature (20 °C). However, there is a relatively good agreement between the measured and modelling results before cooling time, which adds to the validation of the modelling provided by the above comparison with the analytical solutions.

3.2. Crack metric

Fig. 6 is a line profile taken through the centre of the thermal image of the laser spot shown in frame 4 of Fig. 3b. A step change in temperature ($T_R - T_L$), temperature to the right minus temperature to the left of the crack, occurs across the crack and its magnitude characterizes the thermal blocking power of the crack. It is also a measure of the effect that the crack has on thermal
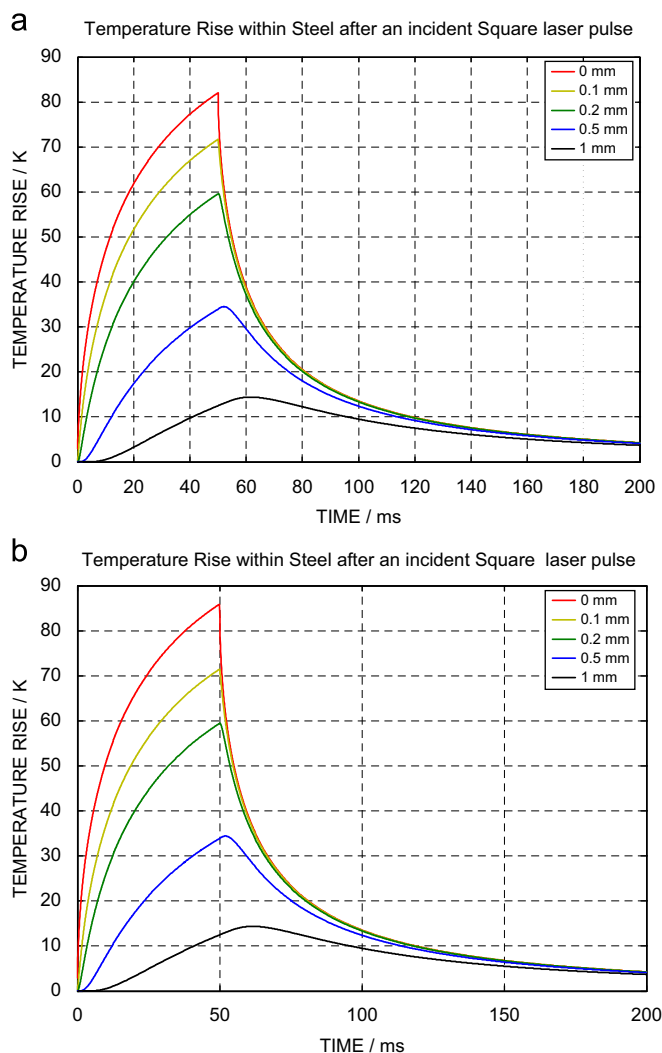
a

b

Fig. 4. (a) 3D analytical modelling results. (b) 3D ghost point finite difference modelling results.

a

b

Fig. 5. (a) Experimental result. (b) 3D ghost point modelling result.

image of the laser spot and, consequently, it may be used to assess the sensitivity of the technique to cracks of varying dimensions. The step temperature change 'metric' is also found to be a function of system operating parameters, as detailed in Sections 3.3 and 3.4.

3.3. Suitable laser power and pulse duration

Important operating parameters are laser power and pulse duration. For laser pulses with the same output energy it is found that the shorter the laser pulse, the higher the temperature difference across the crack. This is a result of the rapid thermal diffusion rate in metals, which causes transient thermal perturbations to dissipate over a shorter time than the duration of the longer pulses. Balanced against this effect is a general increase in crack thermal metric with laser pulse energy. Variations in spatial shape of the laser heating and diameter of the spot can change the distribution of laser energy at the sample surface. However, they are also related with laser output power. In practice, it has been found that good results are obtained in several metal test pieces using a 50 ms pulse duration and laser power in the range 10–21 W, depending on reflectivity of the metal surface. These sample materials include mild steel, stainless steel, titanium alloy and Udimet.
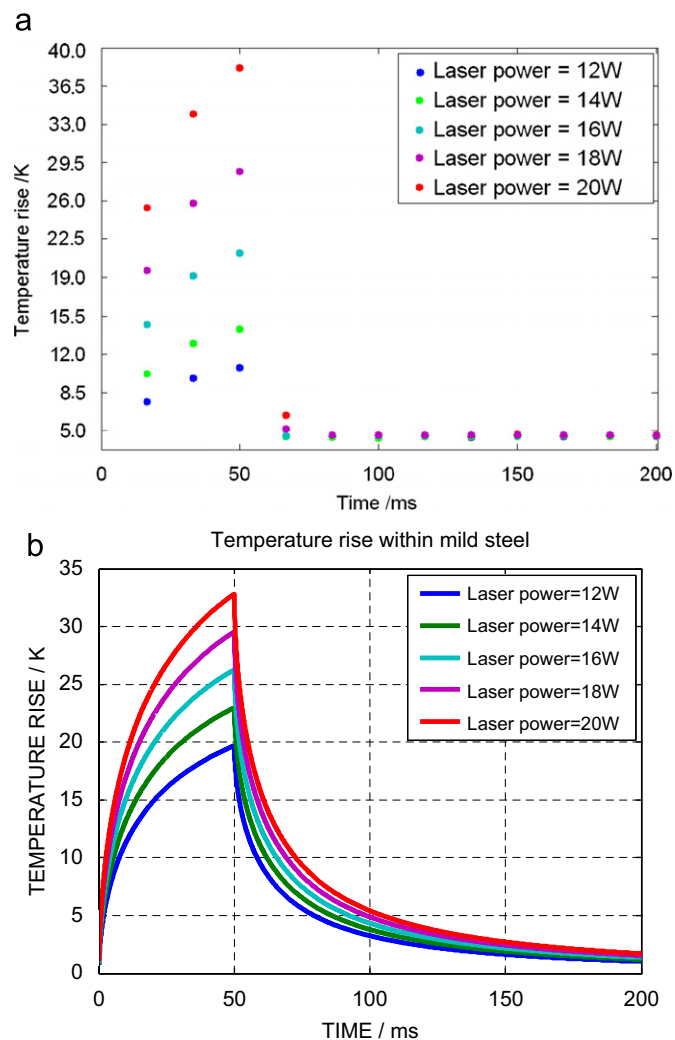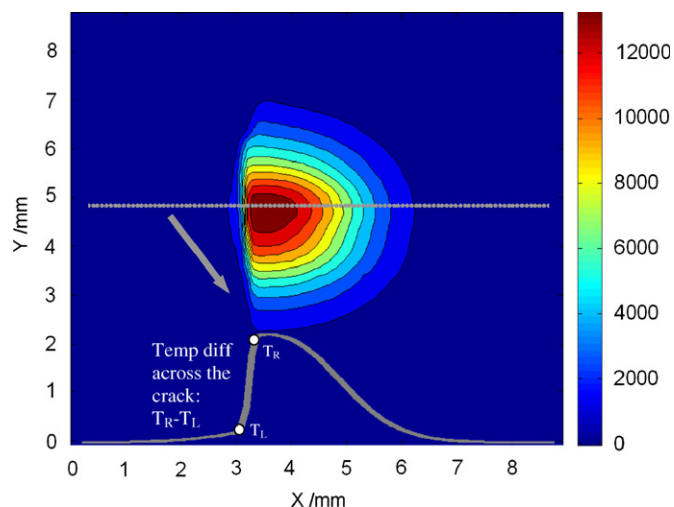

Fig. 6. Frame 4 of Fig. 3b and thermal line profile along line indicated.

3.4. 'Optimum' imaging distance

The 'optimum' imaging distance of the laser spot centre from the crack was also found by both the experiment and the ghost point model. The 'optimum' distance is where the temperature
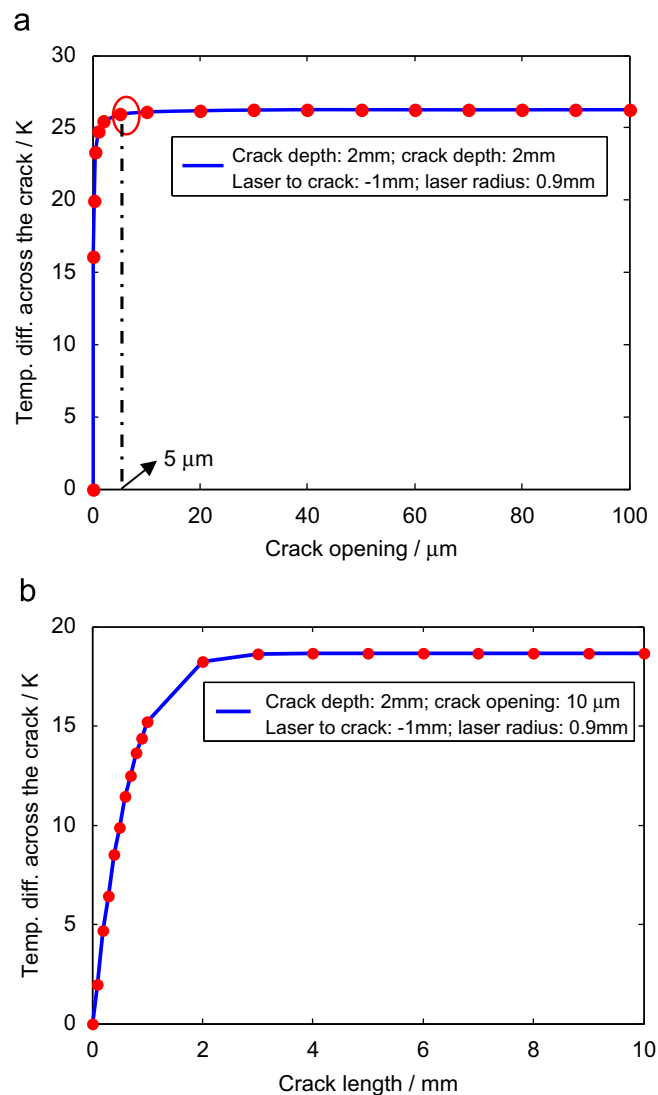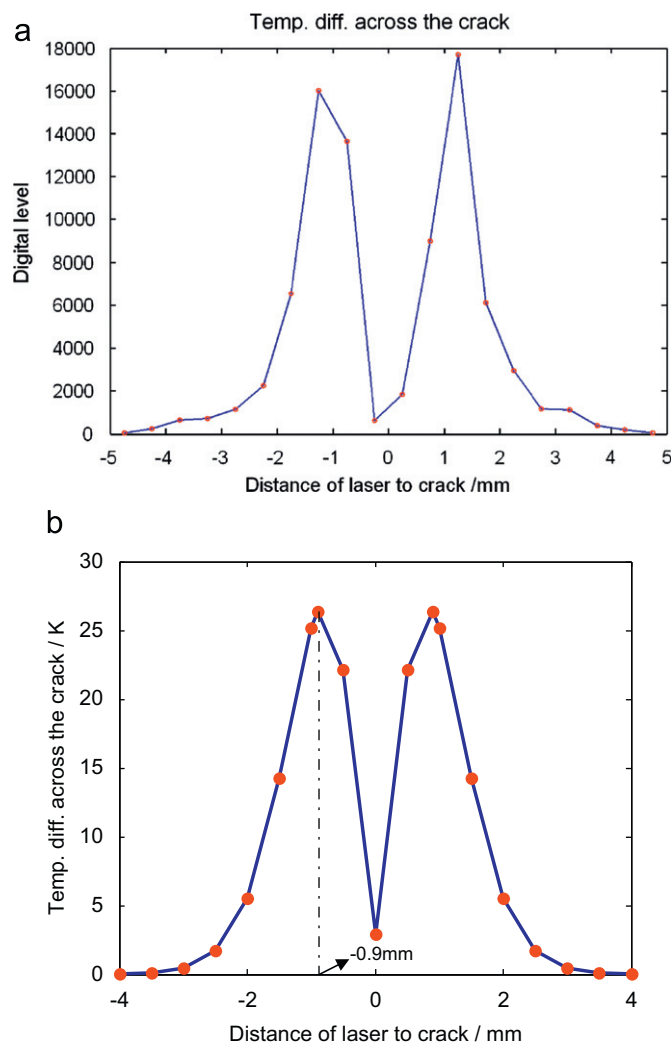
Fig. 7. Temperature differences across the crack when the spot centre has different distances to the crack: (a) experimental results, expressed in IR camera digital levels and (b) modelling results.

difference across the crack has the largest value. Thus the thermal gradient across the crack reaches the largest value too. Fig. 7a shows the maximum temperature difference (near the laser spot centre) across the crack when the spot centre has different distances to the crack (moving along a line through the spot centre perpendicular to the crack). The same test-piece shown in Fig. 3a was used in the experiment. The laser radius was about 1.25 mm. It is shown in Fig. 7a that the maximum temperature difference across the crack occurs at the position when the laser spot centre is 1 beam radius ($1/e$ fall) away from the crack. Fig. 7b shows the modelling result by using the 3D ghost point model. The laser radius was 0.9 mm ($1/e$ fall). Simulated crack opening was 10 μm, length was 2 mm and depth was 2 mm. Temperature difference across the crack reaches the maximum value when the distance of the laser spot centre to the crack was 0.9 mm. The reflectivity of the sample surface was set at 50%. Again, the modelling result shows that the 'optimum' imaging distance is one radius of the spot.

3.5. Variations in crack parameters

Fig. 8a shows modelling results of variations in temperature difference across a crack with different openings in a mild steel block (10 mm × 10 mm × 5 mm). The laser spot radius was

Fig. 8. Dependence of temperature differences across the crack on (a) crack opening, (b) crack length and (c) crack depth.

0.9 mm and the spot was centred at the position near the optimum position, one beam radius from the crack. The laser output power and pulse duration were assumed, respectively, to

be 21 W and 50 ms. The reflectivity of the sample surface was set at 50%. Temperature difference across the crack reaches a plateau value when the opening is larger than 5 μm. Similarly, when changing one of the other crack parameters, crack length or depth, temperature difference across the crack also reaches a plateau value, as shown in Fig. 8b and c. Note here that the residual temperature difference caused by the Gaussian spot profile has been removed. These figures show only the changes caused by the crack. The plateaus occur for crack lengths > 3 mm and crack depths > 2 mm. These results provide an indication of the limits of laser spot imaging for detecting cracks with certain geometries. They also indicate that the technique, theoretically, has a sensitivity adequate for many inspection requirements.

3.6. Effect of crack shape

In reality, cracks present different shapes to the rectilinear slots employed in the basic modelling. Very often, a half-penny shaped crack is formed [16]. Fig. 9 shows an ideal square slot crack and a half-penny crack. Simulation results show that the temperature difference across the crack for a half-penny crack is 1.26 °C smaller than that of a slot crack (lengths of both cracks are 3 mm, openings are 10 μm, in mild steel pieces). The laser output power was 21 W, pulse duration was 50 ms and beam radius was 1 mm. The results were calculated at 0.2 s. Thus, heat blockage effect of the half-penny crack is smaller than that of an ideal slot crack as might be expected. Furthermore, a pouched half-penny crack (smaller openings at crack tips and bottom) can also be simulated, which has smaller temperature difference than that of the half-penny crack by about 0.5 °C under the above situations.

These modelling results show that crack shape can also affect the acquired thermal images and consequent sensitivity of the technique.

3.7. 'Optimum' observation time

There is an 'optimum' observation time at the optimum distance at which the maximum amount of a long crack is revealed. It can be seen in Fig. 3 that the full length of the crack emerges in the later frames. However, if a crack in mild steel is longer than about 3 times of the laser diameter, the signal to noise ratio (SNR) will be poor by the time the heat diffuses to reach the crack tip. Thus, the optimum observation time can be defined as the time when part of the crack, usually with the length within 2–3 diameters of the laser spot (related with the material, the surface situation, etc.), can be observed at the optimum distance. The term 'can be observed' means that the maximum temperature difference across certain part of the crack is at least 6 dB above the noise. For example, in our experiments, the 'optimum'
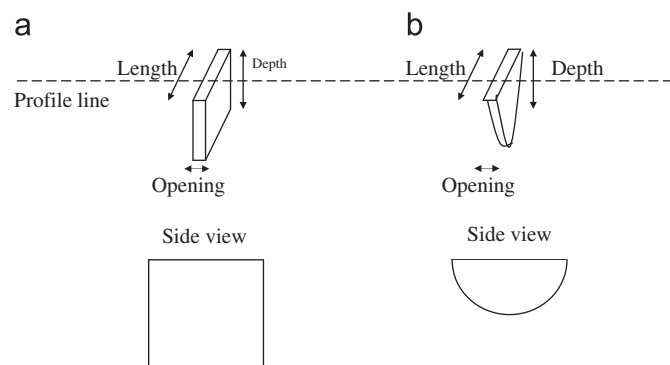
observation time happened at around 200 ms for a 3 mm long, 10 μm wide half-penny crack in an Udimet test-piece. The full extent of longer cracks cannot be satisfactorily imaged by a single laser spot heating but it will be revealed by combining the images obtained on executing a suitable scanning raster.

4. Crack imaging by scanning laser spot

The 3D ghost point model has helped establish the limits of effectiveness of LST in the detection of cracks with opening in the micrometre range. In addition, this 3D model has helped the development of a new crack imaging method. A common image processing technique is to compute the first spatial derivative, which reflects the amplitude change rate in an image and thus extracts edges in images. The perturbation of a laser spot image caused by a crack can be regarded in the same way as an edge feature. However, the background heat flow caused by the focused laser spot is still strong and causes large thermal gradients that are mixed together with the crack effects when the spot is close to the crack. The 'second spatial derivative' was also considered since it can further enhance the edge effect in an image. Fig. 10 shows a simulation of the surface temperature image of a laser heated spot on a stainless steel metal block obtained from the 3D model. The geometry of metal block was 12 mm × 12 mm × 5 mm in x, y and z directions and the modelling grid spacing was 0.1 mm. A 5 mm long half-penny shaped crack was embedded in the grids in the middle of the block. The crack opening was 1 μm. The thermal image, Fig. 10, was obtained 0.15 s after the block was irradiated by a 21 W, 50 ms laser pulse with radius of 1 mm (1/e fall). The laser spot was centred 1 mm to the right of the crack. The temperature profile across the crack and the centre of the spot is also shown in the figure.

Fig. 11a shows the normalized first (blue line) and second (red line) derivatives of the temperature profile line plotted in Fig. 10. The red line in Fig. 11a shows the much improved crack discrimination obtained from second derivative processing. Fig. 11b and c shows normalized 2D images obtained using the first and second derivative image processing of the data shown in Fig. 10 (derivatives taken in the x direction perpendicular to the crack). It is clear that the second derivative processing provides a
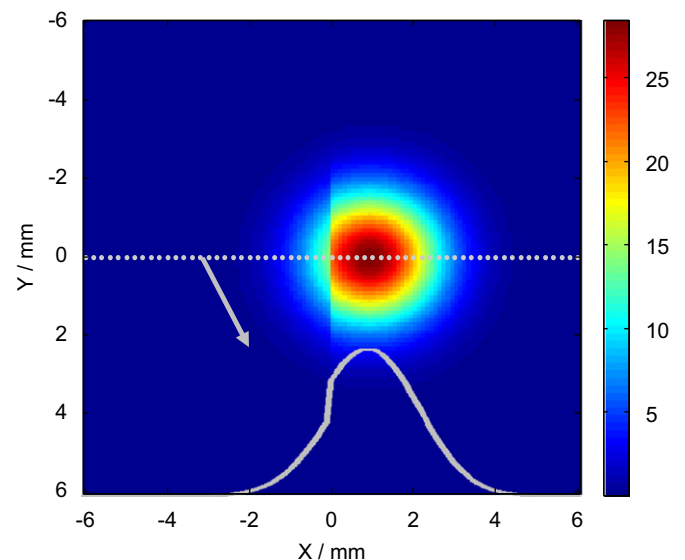

Fig. 9. (a) An ideal slot crack. (b) A half-penny crack.

Fig. 10. Simulated thermal image of a stainless steel sample containing a 5 mm long, 1 μm opening crack at time 0.15 s. The temperature profile across the crack and the centre of the spot is shown in the lower part of the figure.
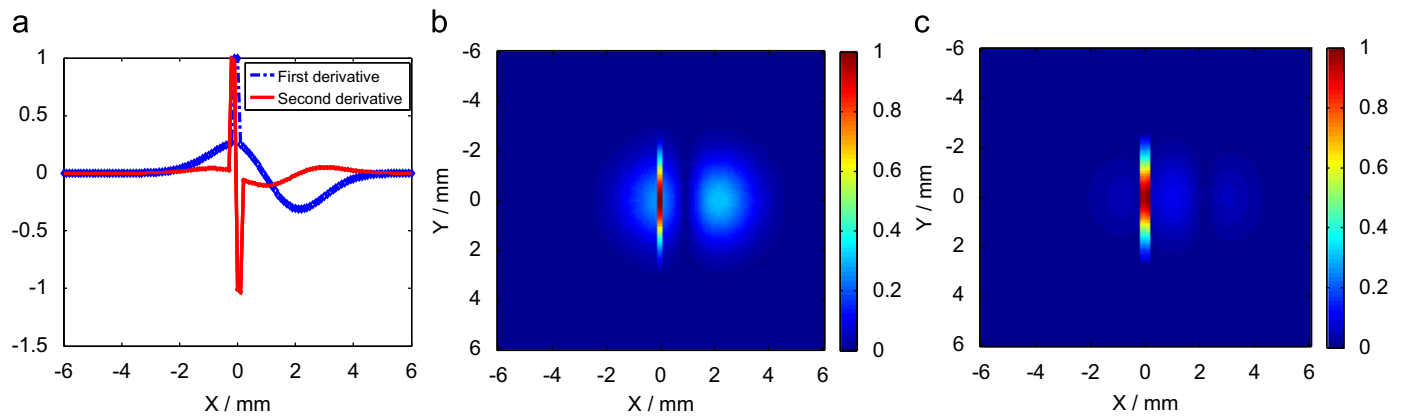
Fig. 11. (a) Normalized first (blue line) and second (red line) derivatives of the temperature profile line in Fig. 10. (b). First derivative image in *x* direction of Fig. 10 image. (b) Second derivative image in *x* direction of Fig. 10 image. (For interpretation of the references to colour in this figure legend, the reader is referred to the web version of this article.)
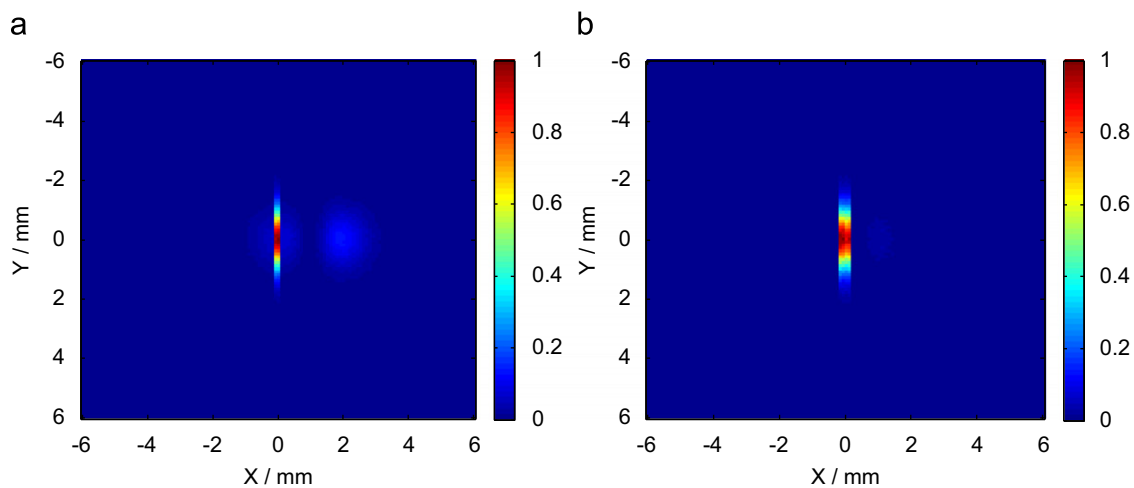

Fig. 12. (a) Summed second derivative image in *x* direction from 0.05 to 0.3 s. (c) Summed second derivative image in *x* direction from 0.05 to 0.3 s.

better means of isolating the image of the crack. The contrast of the crack to the background heat flow (ratio of the maximum amplitude at crack positions to the maximum amplitude of the background heat flow) in Fig. 11b is about 3.21. In Fig. 11c, the contrast becomes 9.79, which is 3.05 times higher than that in Fig. 11b.

In practice, image acquisition time and noise need to be considered. The simulation shown in Fig. 10 corresponds to an image that might be collected by a thermal imaging camera, 0.15 s after the extinction of a laser heating pulse. In practice, more thermal images at different times can be used. This provides the opportunity to form a summed thermal image that will further emphasize the crack structure over the background heat flow. However, the second derivative method is known to be sensitive to noise [17]; hence only thermal images with high signal to noise ratio should be considered. The effects of image addition and noise were investigated by adding ± 0.15 K (one standard deviation) random noise to the above model and summing first and then second derivative thermal images from 0.05 s after the extinction of a laser heating pulse to 0.3 s, when the remaining heating became comparable to the noise level. Images were computed at intervals of 1/60 s matching the 60 Hz frame rate of the IR camera used in the experimental work below. The normalized first and second derivative images are shown in Fig. 12a and b, respectively. After integrating thermal images at different times, the contrast of the crack to the background heat flow in Fig. 12a is 7.23. In Fig. 12b, the

contrast is 27.76, which is 3.8 times higher than that in Fig. 12a. In addition, the integration method improves the contrast by 2.8 times in Fig. 12b compared to Fig. 11c.

The crack length indicated by the single spot images shown in Fig. 10 is about 3.8 mm, which is somewhat shorter than the true 5 mm crack length. In practice the location of a crack might be unknown and a raster scanning technique would be used. A combination of results obtained from such scans will improve the sizing of cracks, as shown in the experimental work below.

A test-piece containing a crack was raster scanned using 21 W, 50 ms laser heating pulses. The laser spot radius was 1 mm (1/*e* fall) and the IR camera field of view was 26.4×20.8 mm². The processing steps performed on the thermal images from the IR camera are as follows:

1. Subtract the background IR image to produce a dark-field image showing only the transient heat diffusion (this can be easily done by subtracting a thermal image obtained before the laser was switched on), and then compute the second derivative of each dark-field image at each scanning step in both *x* and *y* directions. Note here, the dark-field image at each position can be the averaged image of several pre-images taken by the camera before the laser spot is switched on at each position on the specimen surface or any one of the pre-images.

2. Integrate all second derivative images in x or y direction collected from 0.05 to 0.3 s at each scanning position.
3. Form a composite image of all the integrated images obtained at the different scanning positions. A final sum image can be obtained by adding the squares of the two second derivative images in x and y directions to show the derivative information in both x and y directions at the same time.

Fig. 13a shows a dye penetrant inspection (DPI) image of an 11 mm long, 3 mm deep crack with average opening of 24.5 μm in a test-piece (austenitic stainless steel) [18]. The images shown in Fig. 13b and c were obtained using the above image processing methods after scanning the test-piece. Fig. 13b shows the second derivative image in x and Fig. 13c in the y direction. Since the crack was orientated at an angle of approximately 45°, signal amplitudes for the crack in Fig. 13b and c are similar. These crack images are in good agreement with the DPI image of the crack shown in Fig. 13a. Information about crack shape and distribution of crack opening can also be seen in the image; it shows stronger signals in the middle part of the crack, where the crack is most open.

Raster scanning steps of 0.43 mm in the x direction and 0.5 mm in the y direction were used to obtain the images shown in Fig. 13. Investigations were made on the images produced by coarser scanning rasters. The images obtained after increasing scanning steps to 2.58 and 3.44 mm in the x direction are shown in Fig. 14. Most parts of the crack can still be seen using these coarser scanning rasters. This indicates that the crack imaging process may be speeded up by using coarser scanning rasters but it should be recognized that size of the minimum detectable crack will be an increasing function of raster step length.

An image of a smaller, ~8 mm long crack in an Udimet test-piece with an opening of less than 1 μm is shown in Fig. 15. This provides evidence of the remarkable sensitivity of the technique.
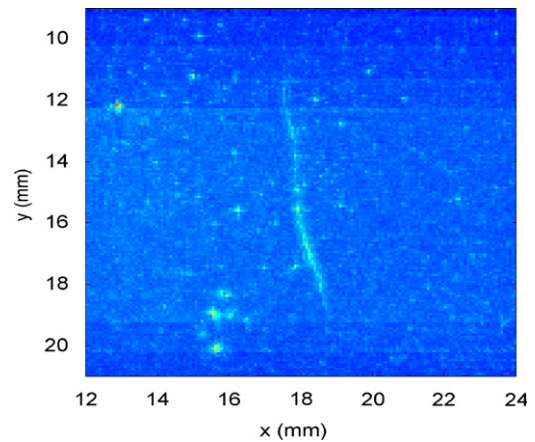

Fig. 15. Summed second derivative image of an 8 mm long crack with opening less than 1 μm.
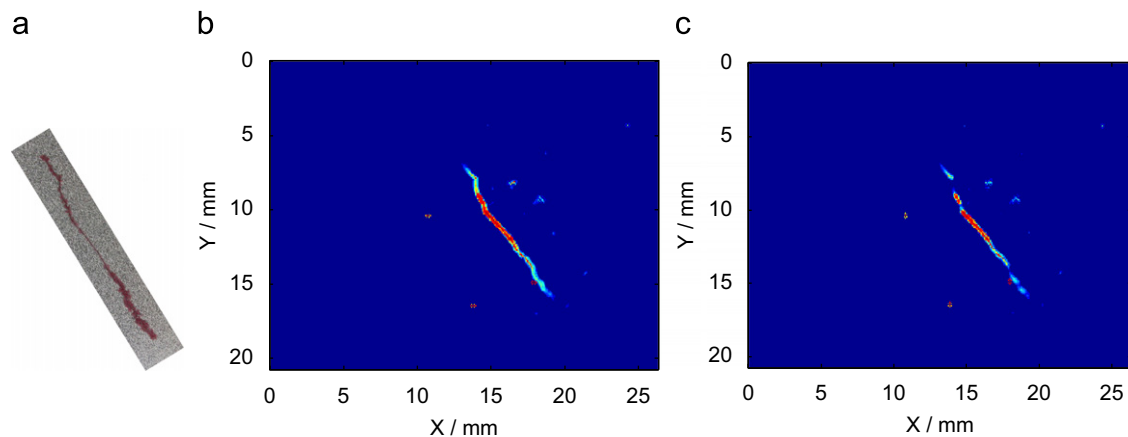

Fig. 13. (a) Dye penetrant image of the crack in the test-piece. (b) Summed second x direction derivative image of the crack. (c) Summed second y direction derivative image of the crack. Scanning steps 0.43 and 0.5 mm in x and y directions, respectively.
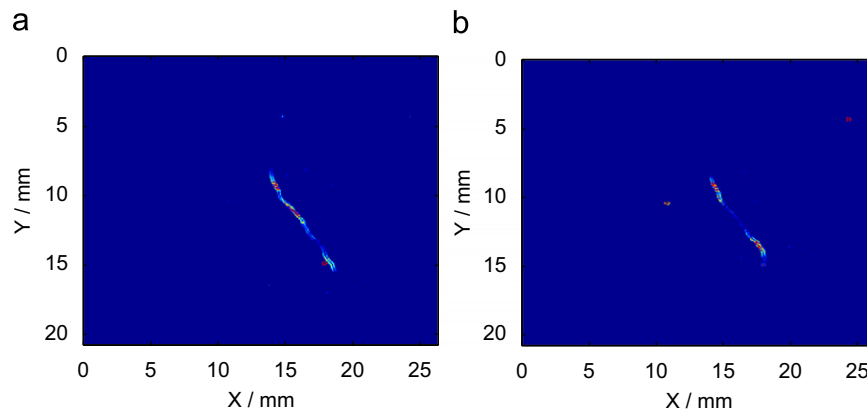

Fig. 14. (a) Summed second derivative image in x direction with scanning step of 2.58 mm. (b) Summed second derivative image in x direction with scanning step of 3.44 mm.

5. Discussion and conclusions

The modelling results presented in this paper indicate the laser spot thermography technique to have a sensitivity to cracks that is competitive with most established NDE techniques. The technique has the advantages of being non-contactive and requiring no surface preparation. However, it is known that for the technique to be successful, surfaces should be clean and free of deep scratches or indentations that would perturb heat flow in a similar manner to a crack. To date, studies have been made only on surface breaking cracks. The ability of the technique to detect cracks beneath coatings is under investigation.

This paper also presents a novel second derivative image processing method for extracting images of cracks after raster scanning. The results obtained show scanned pulse laser spot thermography, incorporating second derivative image processing, to be a new effective nondestructive evaluation technique for detecting and imaging surface breaking cracks with openings in the range of micrometres. Crack images obtained by the new technique are at least comparable to those obtained by the long established DPI method. In addition, this new technique has the advantages of eliminating the long preparation time of the dye penetrant technique, eliminating the use of undesirable liquids, being deployable remotely and being suitable for automation. The practical sensitivity and reliability of the technique are under investigation.

Acknowledgements

References

[1] Reynolds WN. Thermographic methods applied to industrial materials. Can J Phys 1986;64:1150–4.
[2] Milne JM, Reynolds WN. The non-destructive evaluation of composites and other materials by thermal pulse video thermography. Proc SPIE 1984;520:119–22.
[3] Lau SK, Almond DP, Milne JM. A quantitative analysis of pulsed video thermography. NDT&E Int 1991;24:195–202.
[4] Shepard SM, Lhota JR, Ahmed T. Flash thermography contrast model based on IR camera noise characteristics. Nondestr Test Eval 2007;22:113–26.
[5] Sham FC, Chen N, Hong L. Surface crack detection by flash thermography on concrete surface. Insight 2008;50(5):240–3.
[6] Rashed A, Almond DP, Rees DAS, Burrows SE, Dixon S. Crack detection by laser spot imaging thermography. Rev Prog QNDE 2006;26:500–6.
[7] Burrows SE, Rashed A, Almond DP, Dixon S. Combined laser spot imaging thermography and ultrasonic measurements for crack detection. Nondestr Test Eval 2007;22:217–27.
[8] Bantel T, Bowman D, Halase J, Kenue S, Krisher R, Sippel T. Automated infrared inspection of jet engine turbine blades. Proc SPIE 1985;581:18–22.
[9] Devitt J.W., Bantel T.E., Sparks J.M., Kania J.S. Apparatus and method for detecting fatigue cracks using infrared thermography. US Patent 5111048, 1992.
[10] Gruss C, Balageas D. Theoretical and experimental applications of the flying spot camera. In: . 1992; Proceedings of the 27th Eurotherm seminar on quantitative infrared thermography, QIRT. p. 19–24.
[11] Hermosilla-Lara S, Joubert PY, Placko D, Lepoutre F, PiriouM. Enhancement of open-cracks detection using a principal component analysis/wavelet technique in photothermal nondestructive testing. In: Proceedings of the quantitative infrared thermography seminar, QIRT, 2002. p. 41–6 [Archives QIRT 2002-002].
[12] Hermosilla-Lara S, Joubert PY, Placko D. Identification of physical effects in flying spot photothermal non-destructive testing. Eur Phys J Appl Phys 2003;24:223–9.
[13] Krapez JC, Gruss C, Huttner R, Lepoutre F, Legrandjacques L. La camera photothermique—partie I: principe, modelisation, application a la detection de fissures. Instrum Mes Metrol 2001;1:9–39. [in French].
[14] Krapez JC, Lepoutre F, Huttner R, Gruss C, Legrandjacques L, Piriou M, et al. La camera photothermique—partie II: applications industrielles, perspectives damelioration par un nouveau traitement dimage. Instrum Mes Metrol 2001;1:41–67. [in French].
[15] Doyle PA. On epicentral waveforms for laser-generated ultrasound. J Phys D 1986;19(9):1613–23.
[16] Tang Y, Yonezu A, Ogasawara N, Chiba N, Chen X. On radial crack and half-penny crack induced by Vickers indentation. Proc R Soc A 2008;464:2967–84.
[17] Gonzalez RC, Woods RE. Digital image processing. 3rd ed.. New Jersey: Prentice Hall; 2006. p. 702–5.
[18] Trueflaw Ltd., Espoo, Fl-02330, Finland.